Macromolecules

pubs.acs.org/Macromolecules
Article

Solvent-Driven Microdomain Ordering in PI–PS–PMMA Miktoarm Star Polymers

Matus Kalina, Babak Nouri, Merin Joseph, Beate Förster, Martin Dulle, Jonathan M. Gow, Dorthe Posselt, Martin C. Pedersen, Jacob J. K. Kirkensgaard, Gerd E. Schröder-Turk, and Kristoffer Almdal*

Cite This: Macromolecules 2026, 59, 8285–8294

ABSTRACT: The bulk morphology of ABC star polymers composed of polyisoprene (PI), polystyrene (PS), and poly(methyl methacrylate) (PMMA) was investigated, examining the influence of the casting solvent on microphase separation. The lengths of the PI and PS arms were held constant, while the PMMA arm length varied systematically. Small-angle X-ray scattering (SAXS) and scanning transmission electron microscopy (STEM) reveal that solvent choice affects the resulting morphology. Acetone casting induces enhanced long-range order in the sample with the lowest PMMA volume fraction, characterized by a morphology exhibiting both hexagonal and lamellar-like periodicities, consistent with a hexagonally perforated lamella structure. This coexistence persists after thermal annealing, as SAXS profiles show no significant change upon heating and cooling. This behavior indicates a morphology that does not readily reorganize toward a single equilibrium structure, but instead reflects a nonequilibrium morphology resulting from solvent-dependent segregation pathways. Dissipative particle dynamics (DPD) simulations support this interpretation by reproducing pathway-dependent structural transitions.

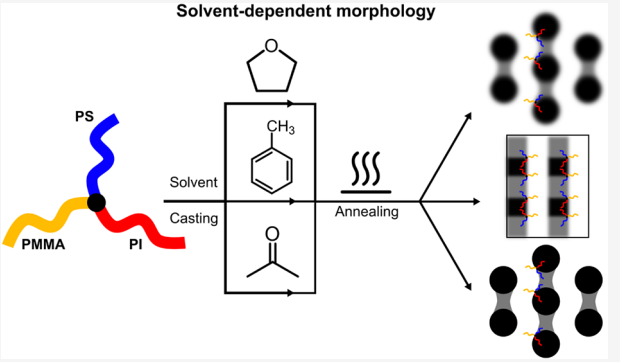

INTRODUCTION

ABC miktoarm star polymers are a specialized subclass of branched copolymers in which three chemically distinct arms are covalently linked to a single junction.[1,2] The combination of three immiscible polymers together with inherent asymmetry and compositional diversity enables access to microphase-separated morphologies that differ substantially from those observed in diblock copolymer systems.[3−7] This increased, architecture driven, morphological diversity reflects the expanded parameter space of ABC systems, which is governed by the overall degree of polymerization N, two independent block volume fractions f_a and f_b, and three pairwise interaction parameters χ_{AB}, χ_{AC} and χ_{BC}.[8] Owing to these features, ABC stars have been examined as model platforms for studying the interplay between architecture, segmental interactions, and packing frustration.[9−11] Despite this fundamental interest, systematic experimental studies have remained limited, mainly due to the challenges associated with controlled synthesis, which requires a precise polymerization protocol and subsequent purification.[12,13]

Among ABC star systems, the PI–PS–PMMA (ISM) is among the more thoroughly studied, partly due to PI and PS being "classical" anionic polymers with well-established reactivity, allowing their synthesis to be reliably controlled.[14−16] In contrast, PMMA historically presented challenges in anionic polymerization, as strongly basic alkyllithium chain ends readily undergo side reactions with the ester functionality, leading to poor control.[17] Subsequent advances in monomer purification and reaction design enabled reliable PMMA polymerization by stabilizing the propagating carbanion, most commonly through the use of 1,1-diphenylethylene (DPE)-based initiators or DPE-functionalized intermediates.[18−23]

The earliest ISM synthesis established a reliable procedure using anionic polymerization and chlorosilane chemistry, producing well-defined ISM stars and demonstrating that the three arms segregate in bulk to form ordered microstructures.[24] Subsequent studies using SAXS and electron microscopy revealed a rich variety of bulk morphologies, including hexagonally packed cylindrical domains, concentric-core structures, and a novel rhombohedral structure.[25] These investigations also showed that the junction points tend to localize along periodically spaced lines where the interfaces

Received: February 24, 2026
Revised: May 12, 2026
Accepted: June 24, 2026
Published: July 6, 2026

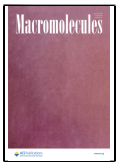

https://doi.org/10.1021/acs.macromol.6c00562
Macromolecules 2026, 59, 8285–8294

Scheme 1. Synthetic Route to the ISM Stars

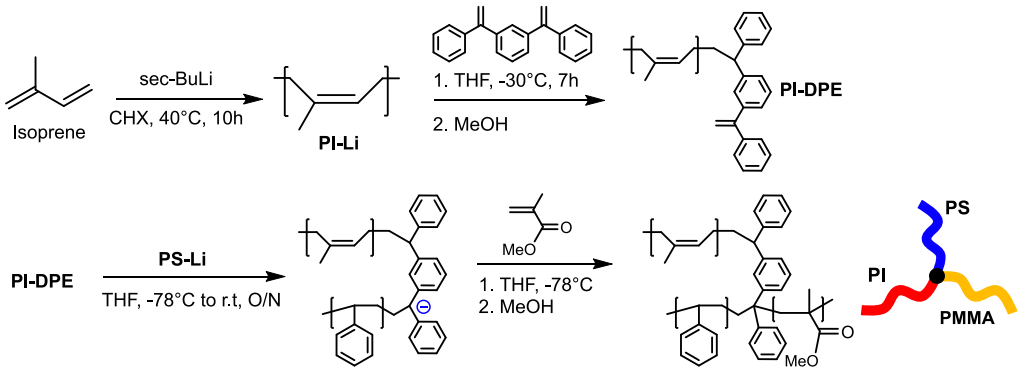

meet.[26] More recent work revisited ISM stars with alternative anionic pathways and examined both bulk and thin-film morphologies, reporting lamellae, hexagonally packed cylinders, and square-packed surface patterns depending on composition and processing conditions.[27] Collectively, these studies highlight the architectural sensitivity and morphological diversity of the ISM system, yet they rely on a limited range of sample histories, principally bulk samples cast from a single solvent followed by thermal, or single solvent annealing.

An important variable therefore remains unexplored: the influence of the casting solvent on the final bulk microstructure after subsequent thermal annealing. ABC stars constrain three chemically distinct arms to meet at one point, which can limit chain mobility and influence equilibration during thermal treatment. As a result, the microdomain arrangement attained during, or immediately after solvent removal can imprint structural biases that are not fully erased during annealing. Although solvent selectivity is known to guide preorganization in other block copolymer systems[28−33] its impact on the bulk morphology of ABC stars has not been investigated. In the ABC architecture, the three arms can exhibit pronounced differences in solubility, hence casting with various solvents may play a crucial role in determining the pretemplating, growth, and ultimately, the final structure.

Here we examine the solvent dependence of bulk microphase separation in a series of five ISM star polymers. Samples were cast from three solvents of differing selectivity, tetrahydrofuran (THF), acetone, and toluene, and subsequently annealed under identical thermal conditions. SAXS and STEM were used to compare the resulting morphologies and assess the extent to which solvent-mediated preorganization influences long-range order. Particular attention is given to cases in which the choice of casting solvent enables access to highly ordered structures not observed under other processing conditions. Dissipative particle dynamics (DPD) simulations were employed to examine whether the observed morphologies can arise from solvent-dependent segregation pathways during casting. These results provide new insight into sample preparation in ABC star systems and demonstrate that sample-solvent history is a critical parameter governing the bulk morphology of ISM stars.

EXPERIMENTAL SECTION

Materials

All chemicals were purchased from Sigma-Aldrich. Sec-butyllithium (1.4 M in cyclohexane) was used as received and titrated by the Gilman double titration method.[34] Isoprene (98%, stabilized), styrene (99%, stabilized), and methyl methacrylate (99%, stabilized) were purified by standard anionic polymerization techniques.[12,18] THF was distilled from purple benzophenone ketyl radical, and cyclohexane (CHX) was distilled from living PS solution. Reactions were performed under argon overpressure in a system described elsewhere.[35]

Synthesis of the ISM Stars. PI−PS−PMMA (ISM) star polymers were synthesized using a DPE-based trifunctional core following previously established routes.[36−38] Living polyisoprene (PI) was prepared in CHX, yielding predominantly 1,4-addition microstructure (95% by ^{1}H NMR), and coupled to the DPE-based core in THF (THF:CHX = 3:1 v/v). Excess core was removed by repeated precipitation from THF into methanol (4x). The resulting polymer was stored at −20 °C. The DPE-terminated PI macroinitiator was reacted with living polystyrene (PSLi) in excess at −78 °C in dry THF to form PI−PS−Li.

MMA was then added portion wise to the living PI−PS anion in THF at −78 °C, withdrawing aliquots between additions to obtain a series of PI−PS−PMMA stars with systematically varying PMMA arm lengths (1:1:x). The products were precipitated to methanol as white powders and analyzed by SEC and ^{1}H NMR spectroscopy.

Homopolymer and PI−PS diblock impurities were removed by CHX extraction and the resulting polymers dried under vacuum. The overview of the synthetic route is shown in Scheme 1. Full synthetic procedures and purification details are provided in the Supporting Information.

CHARACTERIZATION OF THE ISM STARS

Size Exclusion Chromatography (SEC)

Number-average molar masses and dispersities (see Table 1) were determined by SEC using THF as eluent at a flow rate of 1 mL/min at 30 °C. Separations were carried out on a PLGel Mixed-C (Agilent) analytical column equipped with refractive index and dual-angle light scattering detectors. Calibration was performed using narrow-distribution polystyrene standards

Table 1. Characteristics of the ISM Star Polymers

Sample	M_n (g/mol)[a]	Đ[a]	ϕ_I:ϕ_S:ϕ_M[b]	f_I	f_S	f_M
PI	12500	1.12	1:0:0	1	0	0
PS	9300	1.10	0:1:0	0	1	0
PI−PS	21300	1.21	1:0.96:0	0.55	0.45	0
ISM 5−1	37400	1.15	1:0.96:2.1	0.29	0.24	0.47
ISM 5−2	51300	1.14	1:0.96:3.6	0.22	0.18	0.60
ISM 5−3	62900	1.23	1:0.96:5.2	0.17	0.14	0.69
ISM 5−4	73400	1.29	1:0.96:6.7	0.14	0.12	0.74
ISM 5−5	77100	1.43	1:0.96:8	0.12	0.10	0.78

[a]From SEC. [b]From ^{1}H NMR.

https://doi.org/10.1021/acs.macromol.6c00562
Macromolecules 2026, 59, 8285−8294

(Agilent, ReadyCal/EasyCal kits). Data were processed using WinGPC (Agilent).

Nuclear Magnetic Resonance (NMR) Spectroscopy. ^{1}H NMR spectra were recorded in $CDCl_3$ at 400 MHz (Bruker) with a relaxation delay of 10 s. They were used to determine the PI microstructure and to verify arm compositions (volume fraction, f and ratios, ϕ) of the star samples (see Table 1). The spectra are provided in the SI (see Figures S1, S2 and S5−S9)

Small-Angle X-ray Scattering (SAXS). Bulk SAXS samples were prepared by dissolving 7 wt % ISM stars in THF, toluene, or acetone in glass vials. The vials were covered with aluminum foil and perforated with a needle to allow for slow solvent evaporation at room temperature over a period of 1 week under nitrogen atmosphere. The resulting samples were dried under vacuum at room temperature overnight and subsequently annealed at 150 °C for 5 days in a vacuum oven.

The scattering patterns were recorded at Forschungszentrum Jülich with the SAXS system "Ganesha-Air" (SAXSLAB, Xenocs), unless noted otherwise. The X-ray source was a D2-MetalJet (Excillum) with a liquid-metal anode operating at 70 kV and 3.57 mA with Ga−Kα radiation (λ = 0.1341 nm) providing a very small beam (<100 μm). The beam was focused with a focal length of 55 cm using a custom-made X-ray optics (Xenocs). Samples were mounted in 2.1 mm borosilicate glass capillaries (Hilgenberg) or directly on sticky Kapton tape. Unless explicitly noted, all the measurements were performed at room temperature. The scattering data were recorded by a 2D detector working without a beamstop (Eiger 4M, Dectris) with sample-to-detector distance of 1860 mm, covering the range of scattering vectors, q, between 0.05 and 3 nm^{-1}. The azimuthally averaged data were normalized to incident beam, counts per solid angle and measurement time before subtraction of a scattering spectrum from Kapton as background.

Synchrotron SAXS measurements were performed at the SAXSMAT P62 beamline (DESY, Hamburg).[39] Samples were mounted in 2.1 mm borosilicate glass capillaries (Hilgenberg) and analyzed at room temperature. Data were collected using λ = 0.095 nm and a sample-to-detector distance of 2500 mm, providing an accessible q-range of 0.16−4.2 nm^{-1}. Two-dimensional scattering patterns were azimuthally integrated to obtain intensity profiles $I(q)$.

Supplementary investigations were performed at RUCSAXS, Roskilde University Interdisciplinary Scattering X-ray hub.

Scanning Transmission Electron Microscopy (STEM). Samples were embedded in epoxy resin (EpoTek 301, Epoxy Technology), cured overnight at 40 °C, and trimmed using Leica EM Trim2 trimming machine. Ultrathin sections of the samples were produced at room temperature using a Leica Ultramicrotome EM UC7 with a 35° diamond knife (DiAtome). These sections, approximately 90 nm thick, were floated on a water bath and transferred to a carbon-coated copper grid (Science Services). The samples were stained with OsO_4 (4% in H_2O, Science Services) for 2 h followed by RuO_4 ($RuCl_3$ mixed with NaOCl) for 15 min to stain PI and PS domains respectively. Electron microscopy images were taken with a Thermo Fisher Volumescope Scanning Electron Microscope equipped with a field emission gun (FEG) operating at 30 kV, using a STEM 3+ detector in bright-field mode at a working distance of 7−8 mm. Images were processed using ImageJ.[40]

Dissipative Particle Dynamics (DPD) Simulations. ISM stars were represented using a coarse-grained bead−spring model, in which the three arms were connected to a neutral junction bead.[41] Interactions between beads were described by interaction parameters a_{ij}, related to experimental Flory−Huggins interaction parameters via the relation $a_{ij} = a_{ii} + 3.497\,\chi_{ij}$,[42] such that the asymmetric incompatibility between PI, PS, and PMMA was retained. Like−like interaction parameters were set equal. The unlike interaction parameters were calculated from the rescaled χ values and then uniformly scaled (eq 1 in Supporting Information) because the initial values were too low to produce segregation in the DPD simulations,[43] preserving the relative interaction hierarchy between block pairs. DPD simulations were conducted using HOOMD-blue package.[44] Visualizations were created using VMD.[45]

Simulations were carried out in a cubic box with particle density ρ = 3. The initial configurations consisted of randomly distributed ISM molecules. To establish a homogeneous starting state, all interaction parameters were initially set equal prior to activating selective repulsive interactions to induce phase separation. The system was then evolved until steady morphology was reached.

RESULTS AND DISCUSSION

The molecular characteristics of the 5 ISM star polymers, forming the primary set examined in this work, are summarized in Table 1.

The ISM samples exhibit monomodal SEC traces with relatively narrow dispersities (Đ = 1.1−1.4, Figure S4). ^{1}H NMR spectroscopy was used to confirm the polymer arm compositions, using the following polymer densities for the volume fraction calculations: ρ_{PI} = 0.91 g cm^{-3},[46] ρ_{PS} = 1.05 g cm^{-3},[47] and ρ_{PMMA} = 1.19 g cm^{-3}.[47] No detectable homopolymer impurities remained after residual homopolymer/diblock extraction (Figure S3).

Effect of Casting Solvent on Bulk Ordering

Solvent-mediated preorganization is well established in block copolymers[48−51] where selective solvation can bias specific microdomain formation during solvent evaporation. In ABC stars, structural relaxation is further hindered because the three polymer arms are bound together at a junction point that is expected to reside along the domain interfaces, such that large-scale rearrangement requires collective motion of multiple blocks rather than independent chain diffusion. This constraint can slow the rearrangement and contribute toward preservation of morphologies established during solvation and solvent removal, allowing solvent-imprinted structures to persist even after thermal annealing.

In previous ISM studies, THF was used as solvent,[27] providing relatively nonselective solvation for all three blocks. Chloroform has also been used as a casting solvent[25,26] but the solvent-morphology relationship was not examined in these studies. In this work, to probe the effect of solvent more directly, THF, toluene and acetone were chosen as casting solvents: toluene is comparatively more selective for PI and PS, whereas acetone is more selective for PMMA, as shown in Table 2. An overview of the SAXS profiles obtained after casting from THF, toluene and acetone is shown in Figure 1.

The SAXS profiles highlight that the response to casting solvent is composition-dependent. While, with choice of solvent, shifts in the first-order peak position, corresponding

https://doi.org/10.1021/acs.macromol.6c00562
Macromolecules 2026, 59, 8285−8294

Table 2. Solubility Parameters of the Respective Solvents and Polymer Blocks

Component	Solubility parameter[a] $(MPa)^{1/2}$
Toluene	18.2
THF	18.6
Acetone	20.3
cis-1,4-PI	16.2−16.8
PS	17.8−18.7
PMMA	19[b]−22.7[a]

[a]Common solubility parameter ranges in ref 52. [b]Ref 25.

to changes in the characteristic domain spacing, are observed for all samples, pronounced order, evidenced by well-resolved higher-order SAXS features, is only clearly observed for ISM 5−1 (Figure 1, panel a), where acetone casting results in the appearance of additional higher-q features. At longer PMMA arm content, this behavior is not observed: for ISM 5−2, THF-cast films exhibit local ordering in STEM despite broader SAXS features (see Figure 4), whereas acetone and toluene-cast films display significantly more disordered microstructures (Figure S14). For samples with longer PMMA arms (ISM 5−3 to ISM 5−5), no improvements in ordering are observed for acetone or toluene casting; instead, THF-cast samples display small ordered domains in a disordered matrix in STEM (Figures S15−S18). These observations are consistent with increasing PMMA chain length progressively slowing down the chain dynamics, such that longer annealing times may be required to reach an equilibrium.[53]

The strong ordering observed for the acetone-cast ISM 5−1 is notable, given the relatively low interaction parameters in this system. Reported values are on the order of $\chi_{IM} \approx 0.08$,[54] at room temperature, with $\chi_{IS} \approx 0.05$, $\chi_{SM} \approx 0.02$, at 150 °C,[55]

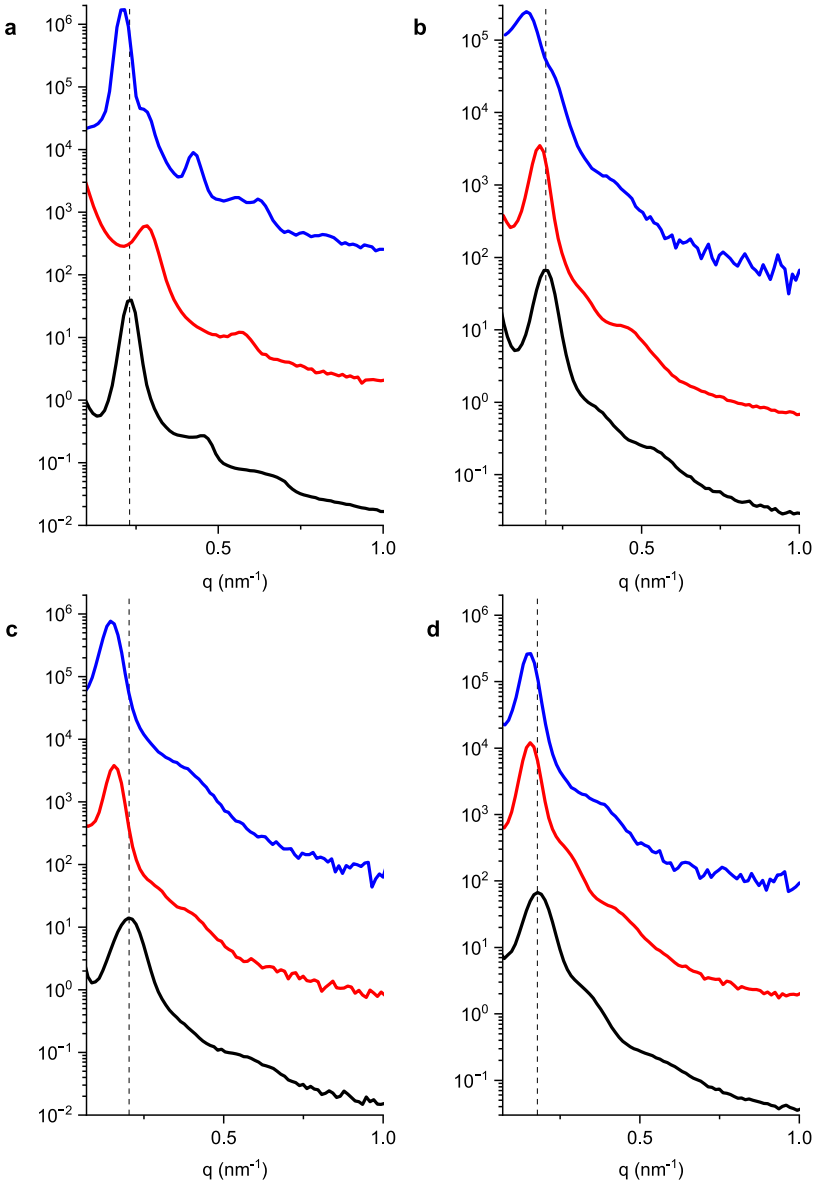

Figure 1. SAXS profiles of (a) ISM 5−1, (b) ISM 5−2, (c) ISM 5−3, and (d) ISM 5−4 cast from THF (black), toluene (red), and acetone (blue), followed by thermal annealing at 150 °C for 5 days. Curves are vertically offset for clarity. Vertical dashed lines indicate the first-order peak position of the THF-cast sample to highlight shifts in scattering vector, q*. ISM 5−5 not included due to the absence of order under these conditions (see Figures S17 and S18).

https://doi.org/10.1021/acs.macromol.6c00562
Macromolecules 2026, 59, 8285−8294

all defined using a reference segment volume of 0.1 nm^3.[27] As these values originate from different temperature regimes, they are used here only to compare the relative favorability of interactions between block pairs. To improve peak resolution, the acetone-cast ISM 5−1 was remeasured at a synchrotron SAXS beamline, with the corresponding profile shown in Figure 2.

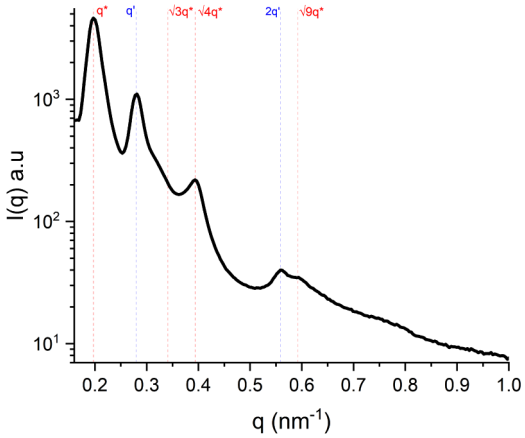

Figure 2. SAXS profile of acetone-cast ISM 5−1, annealed at 150 °C for 5 days. Dashed vertical lines indicate the positions of two characteristic scattering vectors: the first-order peak q* and its higher-order reflections (red), and a second first-order peak q' with its corresponding reflections (blue).

The SAXS profile of acetone-cast ISM 5−1 exhibits a well-defined first-order peak at $q^* \approx 0.197$ nm^{-1}, accompanied by several higher order reflections. If the pattern is indexed assuming a single fundamental length scale, resulting peak ratios ($\sqrt{2}$, $\sqrt{3}$, $\sqrt{4}$, $\sqrt{8}$, $\sqrt{9}$) are largely consistent with a bicontinuous, cubic $Pn\bar{3}m$ structure. However, direct imaging does not support this assignment, indicating that single-lattice indexing is not an appropriate description of the observed scattering profile.

Closer examination of the peak positions suggests the presence of more than one characteristic periodicity. In addition to the primary reflection at q*, a second first-order peak at $q' \approx 0.281$ nm^{-1} with a corresponding feature at $2q'$ indicates the presence of an additional structure, which indicates either coexistence of distinct ordered structures or a single morphology with two separate domain spacings. The corresponding two-dimensional SAXS pattern is isotropic (Figure S11), indicating the absence of a preferred orientation and suggesting that these features do not arise from alignment effects. To further clarify the structural origin of the reflections, STEM was used to directly probe the morphology of acetone-cast ISM 5−1 films, shown in Figure 3.

STEM imaging of acetone-cast ISM 5−1 films reveals distinct structural motifs that account for the proposed multilength-scale SAXS features. In addition to extended lamellar regions consistent with the second SAXS length scale (panel a), large areas exhibit domains arranged with hexagonal symmetry (panels b−d). The primary SAXS peak corresponds to $d^* = 31.9$ nm, which for hexagonal packing yields a lattice parameter $a = 36.8$ nm. Center-to-center spacings measured from STEM are in the range of 30−37 nm, consistent with local lattice distortion and projection effects. The broader spacing range observed by STEM likely reflects not only

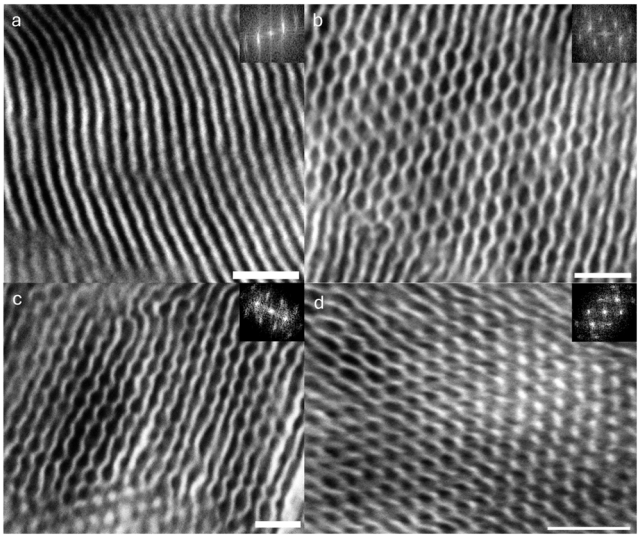

Figure 3. STEM images of acetone-cast ISM 5−1, annealed at 150 °C for 5 days. Panel (a) highlights a lamellar-like region with a distinct periodicity. Panels (b−d) show regions with hexagonally arranged PI domains. Insets show the corresponding fast Fourier transforms (FFT). Scale bars: 100 nm. PI (OsO_4): black, PS (RuO_4): gray, PMMA: white.

projection effects related to sectioning direction, but also compression of the ultrathin sections during microtomy, which can introduce slight distortion in the real-space images and corresponding FFT patterns.

Dark regions correspond to PI domains, while the surrounding PMMA regions exhibit a continuous morphology that curves around and locally perforates these domains (see bottom of panel 3c). This arrangement is indicative of minimization of unfavorable PI−PMMA contacts. The PS block does not form a visually distinct domain, but instead appears to localize at the PI/PMMA interface, in line with its comparatively lower interaction parameter with PMMA, acting as an interfacial mediator. This behavior has been shown in earlier studies on ISM star polymers, which showed that the star architecture enables selective avoidance of unfavorable block−block contacts, allowing the molecule to effectively "choose" which arms interact directly.[26] Importantly, the additional periodicity observed does not correspond to the primary domain spacing, but instead reflects a second, independent length scale, consistent with well-defined lamellar regions with a uniform spacing of 22 ± 0.5 nm, in agreement with the $d' = 22.4$ nm derived from SAXS ($q' = 0.281$ nm^{-1}). Similar perforated structures have been reported in related systems as long-lived, nonequilibrium morphologies that persist even after extended annealing up to several weeks.[56−58]

Given that acetone is the least favorable solvent for PI, the morphology is likely established during solvent evaporation, where PI domains segregate early within a PS/PMMA-swollen matrix. The star junction constrains subsequent rearrangement by keeping PS and PMMA in close proximity during thermal annealing, which promotes PS enrichment at the PI/PMMA interface. Upon further annealing, partial PS/PMMA segregation occurs, giving a three-component morphology with PS at the PI/PMMA interface and partially mixed within the PMMA matrix.

The pronounced acetone-induced ordering observed for ISM 5−1 is not universal across the series. For ISM 5−2, the

https://doi.org/10.1021/acs.macromol.6c00562
Macromolecules 2026, 59, 8285−8294

most ordered microstructure is instead obtained for THF-cast films, where STEM reveals extended regions of local hexagonal packing (Figure 4). In contrast to ISM 5−1, the corresponding

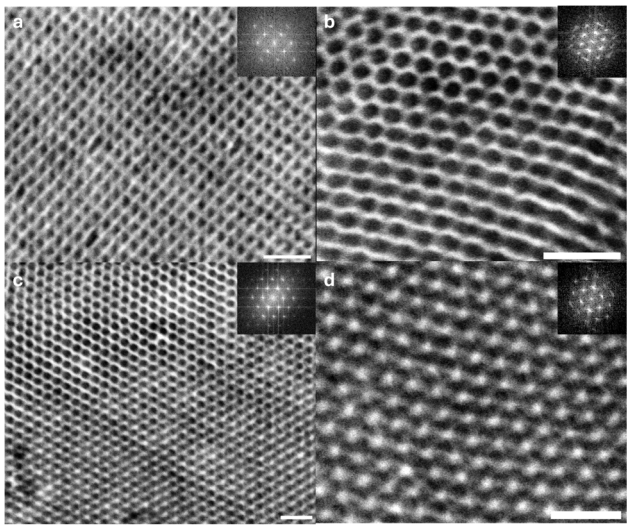

Figure 4. STEM images of THF-cast ISM 5−2, annealed at 150 °C for 5 days, showing extended regions of local hexagonal packing (a-d). Insets show the corresponding FFT. Scale bars: 100 nm. PI (OsO_4): black, PS (RuO_4): gray, PMMA: white.

SAXS features for ISM 5−2 remain broader and less decisive, consistent with a reduced correlation length despite locally well-defined packing in real space. The observed reflections are consistent with higher-order peaks expected for hexagonal symmetry (see Figure S12). Acetone and toluene-cast ISM 5−2 films show substantially more disordered morphologies (Figure S14), underscoring that solvent effects depend strongly on arm length ratio rather than following a universal hierarchy.

In THF-cast ISM 5−2, the hexagonal packing is comparatively less distorted than in acetone-cast ISM 5−1, with more rounded PI domains and reduced curvature of the surrounding PMMA regions. PS remains localized at the PI/PMMA interface (panel b). Because THF solvates all three blocks relatively well, solvent removal is less strongly biased toward early collapse of a single component, which may reduce the extent of interfacial frustration and yield more regular local packing. Notably, PMMA domains now appear as discrete, finite features rather than continuous sheets (panel d), though it should be noted that the observed inversion is gradual, not abrupt, as seen in panel c. The corresponding FFTs indicate predominantly hexagonal ordering, although slight distortions from ideal 6-fold symmetry are evident in panel (a).

Because the final morphologies depend on casting history and do not fully converge under identical annealing conditions, the structures likely reflect the pathway followed during solvent evaporation and subsequent relaxation. DPD simulations were therefore used to follow this dynamic process and examine whether the ABC star architecture can produce multi length-scale morphologies.

DPD Simulations

Simulations were performed for the ISM 5−1 and ISM 5−2 systems, using bead numbers (N_I, N_S, N_M) = (5, 5, 11) and (5, 5, 18), respectively, to reproduce the arm proportions of the experimental systems, where I = PI, S = PS and M = PMMA. These systems were selected as they were the only compositions exhibiting clear long-range order. Like−like interaction parameters were set equal for all components (a_{II} = a_{SS} = a_{MM} = 25),[59] while unlike interaction parameters were uniformly scaled (eq 1, Supporting Information) to retain the asymmetric incompatibility of the ISM system, while preserving the relative hierarchy: $a_{IM} > a_{IS} > a_{SM}$. The final values were (a_{IM} = 40, a_{IS} = 36, a_{SM} = 29). Simulations were carried out in cubic boxes of varying size and with independent random initial configurations to verify that the resulting morphologies were not dependent on system size or initialization. Representative results are shown for box sizes of 23^3 for ISM 5−1 and 31^3 for ISM 5−2.

Solvent effects were incorporated implicitly by introducing selective ramping of the repulsive interaction parameters during the simulation. Rather than modeling solvent molecules, selectivity was represented through the order in

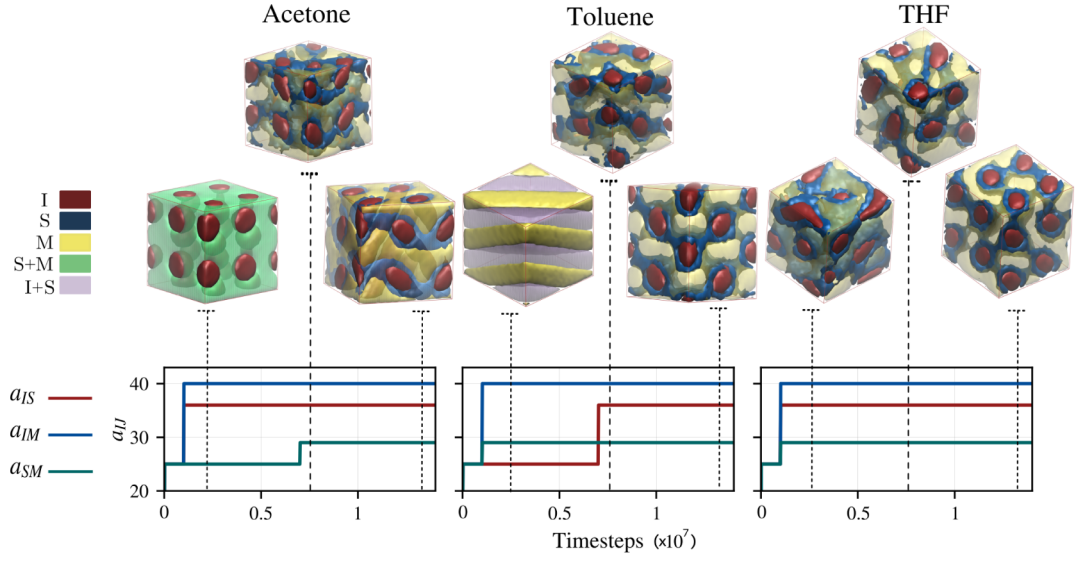

Figure 5. Time evolution snapshots for ISM 5−1 shown for three casting scenarios. Corresponding evolution of interaction parameters is plotted for each case. The matrix components (M, S+M, I+S) are rendered with reduced transparency to highlight the underlying morphologies.

https://doi.org/10.1021/acs.macromol.6c00562
Macromolecules 2026, 59, 8285−8294

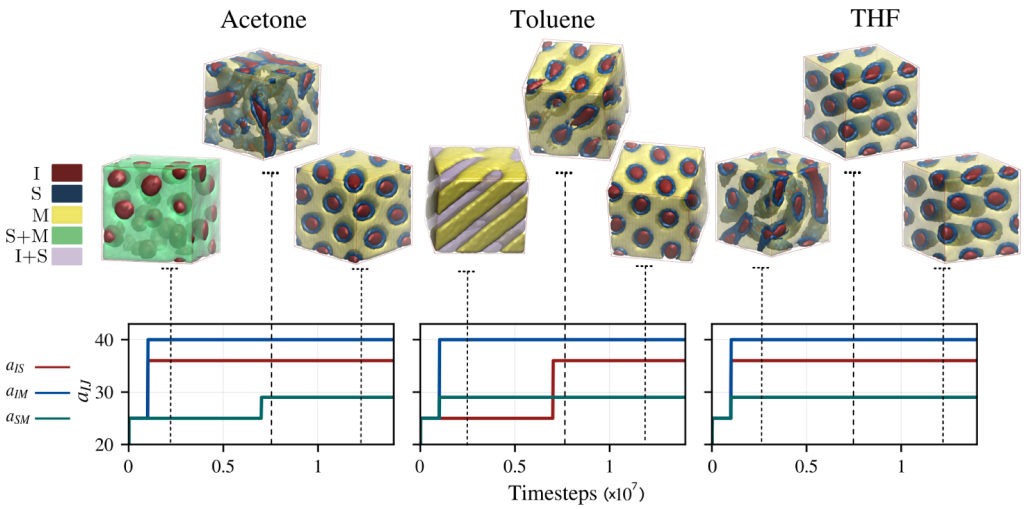

Figure 6. Time evolution snapshots for ISM 5−2 shown for three casting scenarios. Corresponding evolution of interaction parameters is plotted for each case. The matrix components (M, S+M, I+S) are rendered with reduced transparency to highlight the underlying morphologies.

which segregation between components was activated, based on the inferred relative affinities of PI, PS, and PMMA toward the casting solvents. In the first stage, the component least compatible with the chosen solvent segregates from a homogeneous mixture. In the second stage, phase separation between the remaining components proceeds within the bulk as the effective incompatibility between all blocks increases.

Based on this approach, three solvent-mimicking scenarios were considered to reflect the experimental casting conditions. For *Acetone*, PI was treated as the least solvated component and segregated first, followed by PS−PMMA separation. For *Toluene*, PMMA segregated first, reflecting its comparatively poorer solvation. For *THF*, all interaction parameters were increased simultaneously, representing relatively nonselective solvation and providing a reference case corresponding to single-step segregation. The resulting time evolution of domain formation for these three scenarios in ISM 5−1 is shown in Figure 5.

In the *Acetone* case, after the IM and IS interaction parameters are ramped up, PI domains emerge within a mixed PS/PMMA matrix. Interestingly, this transition appears to proceed through a BCC sphere-like arrangement, although this was not verified experimentally. Upon activation of the remaining repulsive interaction, separation between PS and PMMA occurs, leading to further reorganization. During this stage, the PI domains merge and elongate, forming core−shell cylindrical structures with PS occupying the interfacial region and PMMA being the surrounding matrix.

The *Toluene* case represents the conceptual opposite of acetone. In this case, PMMA is the least solvated component and segregates first when PMMA-related interaction parameters, a_{SM} and a_{IM}, are increased. At this stage, PMMA domains emerge and organize into lamellae, with PMMA alternating with mixed PI/PS regions. Upon activation of the remaining IS interaction, separation between PI and PS proceeds, leading once again to the formation of PI−PS core−shell cylinders embedded within a discrete PMMA matrix. Notably, this final morphology was not observed experimentally, with only lamellar ordering present in the toluene-cast sample.

For *THF*, all components are treated as similarly solvated, and all of the repulsive interactions are increased simultaneously. While THF is not strictly nonselective, its relative preference toward any single component is weaker compared to acetone and toluene, and is therefore represented here by a single-step increase in segregation strength. As a result, segregation proceeds through a single transition without an intermediate stage dominated by one component. The system evolves directly from the homogeneous state into core−shell cylindrical structures similar to the late-stage morphologies observed in the other pathways.

For the ISM 5−2 system, shown in Figure 6, a comparable evolution toward core−shell cylinders is observed across all scenarios. Although the intermediate transition states differ depending on the order of segregation, the final morphologies converge toward similar cylindrical arrangements, indicating that the primary effect of solvent selectivity lies in the assembly pathway rather than in the resulting equilibrium-like structure. However, experimentally, a similar cylindrical morphology was only observed in the THF-cast sample.

While the DPD simulations consistently produce well-defined core−shell cylindrical structures, such complete shell formation is not directly observed experimentally. In the STEM images, PS is clearly enriched at the PI/PMMA interface, but it is unclear whether it forms a uniform layer covering the entire surface of the PI domains or instead assembles into more discrete interfacial domains. This difference is likely related to the level of coarse-graining inherent to the DPD model, in which each component is represented by uniform interaction parameters and interfacial structure is therefore simplified relative to the experimental system. In contrast, the experimental system involves additional factors not captured in the simulations, including local compositional fluctuations, chain polydispersity, and kinetic constraints during solvent evaporation, all of which may disrupt the formation of continuous interfacial layers. Because the present DPD model does not capture glassy dynamics, it may further underestimate kinetic trapping effects that contribute to the persistence of nonequilibrium morphologies in the experimental system.

Despite these differences, the simulations reproduce the key qualitative feature observed experimentally, especially regarding the pathway dependence of the resulting morphology. Although the DPD simulations ultimately converge to single well-defined structures, they pass through distinct intermediate

https://doi.org/10.1021/acs.macromol.6c00562
Macromolecules 2026, 59, 8285−8294

states during staged segregation. This suggests that, under experimental conditions, different regions of the sample may become kinetically trapped at different stages of this transition, giving rise to the observed coexistence of structures. The DPD simulations support the interpretation that solvent-dependent ordering in the ISM system is governed primarily by the sequence of segregation during film formation, while the finer structural details of interfacial organization remain sensitive to molecular-level effects, which are beyond the resolution of the coarse-grained model.

CONCLUSION

Taken together, our results demonstrate that solvent selectivity can play a decisive role in directing bulk ordering in ABC star polymers. In the present ISM system, acetone casting induces a solvent-imprinted morphology characterized by multiple periodicities, exhibiting both hexagonal and lamellar-like features, consistent with hexagonally perforated lamellar structures in a nonequilibrium state. The persistence of these metastable structures following thermal annealing (see Figure S10) highlights the importance of kinetic constraints imposed by the star architecture and the differential solubility of the individual blocks in the casting solvent. The resulting morphology is largely established during film formation, with solvent-selective casting promoting preorganized domain arrangements that are not fully equilibrated during annealing. These findings underscore solvent history as a relatively simple tunable parameter for accessing nonequilibrium morphologies in ABC star systems. More broadly, they suggest that pathway control during processing may offer a route to structural states that are not easily accessible through thermal annealing alone.

ASSOCIATED CONTENT

Supporting Information

The Supporting Information is available free of charge at https://pubs.acs.org/doi/10.1021/acs.macromol.6c00562.

Experimental details for polymer synthesis, additional ^{1}H NMR and SEC chromatograms, additional SAXS scattering data, STEM images of the remaining samples and DPD parameters (PDF)

AUTHOR INFORMATION

Corresponding Author

Kristoffer Almdal − *Department of Chemistry, Technical University of Denmark, Kgs. Lyngby 2800, Denmark;* orcid.org/0000-0002-5490-9303; Email: kral@dtu.dk

Authors

Matus Kalina − *Department of Chemistry, Technical University of Denmark, Kgs. Lyngby 2800, Denmark;* orcid.org/0009-0005-5005-9857

Babak Nouri − *Department of Chemistry, Technical University of Denmark, Kgs. Lyngby 2800, Denmark*

Merin Joseph − *Department of Chemistry, Technical University of Denmark, Kgs. Lyngby 2800, Denmark; Niels Bohr Institute, University of Copenhagen, Copenhagen 2100, Denmark;* orcid.org/0000-0002-0441-9365

Beate Förster − *Ernst-Ruska Centre for Microscopy and Spectroscopy with Electrons (ER-C-1), Forschungszentrum Jülich, Jülich 52425, Germany;* orcid.org/0000-0002-8464-4473

Martin Dulle − *Centre for Neutron Scattering and Soft Matter (JCNS-1), Forschungszentrum Jülich, Jülich 52425, Germany*

Jonathan M. Gow − *IMFUFA, Department of Science and Environment, Roskilde University, Roskilde 4000, Denmark*

Dorthe Posselt − *FRUSTMI, IMFUFA, Department of Science and Environment, Roskilde University, Roskilde 4000, Denmark*

Martin C. Pedersen − *Niels Bohr Institute, University of Copenhagen, Copenhagen 2100, Denmark;* orcid.org/0000-0002-8982-7615

Jacob J. K. Kirkensgaard − *Niels Bohr Institute, University of Copenhagen, Copenhagen 2100, Denmark; Department of Food Science, University of Copenhagen, Copenhagen 1958, Denmark;* orcid.org/0000-0001-6265-0314

Gerd E. Schröder-Turk − *School of Mathematics, Statistics, Chemistry and Physics, Murdoch University, Perth WA 6150, Australia*

Complete contact information is available at: https://pubs.acs.org/10.1021/acs.macromol.6c00562

Notes

The authors declare no competing financial interest.

ACKNOWLEDGMENTS

The Novo Nordisk Foundation is gratefully acknowledged for funding the project (NNF22OC0075180) and RUCSAXS, the Roskilde University Interdisciplinary X-ray Scattering Hub (NNF21OC0068491).

ABBREVIATIONS

CHX	Cyclohexane
DPD	Dissipative Particle Dynamics
DPE	1,1-Diphenylethylene
NMR	Nuclear Magnetic Resonance
PI	Polyisoprene
PS	Polystyrene
PMMA	Poly(methyl methacrylate)
SAXS	Small-angle X-ray Scattering
SEC	Size Exclusion Chromatography
STEM	Scanning Transmission Electron Microscopy
THF	Tetrahydrofuran

REFERENCES

(1) Fujimoto, T.; Zhang, H.; Kazama, T.; Isono, Y.; Hasegawa, H.; Hashimoto, T. Preparation and characterization of novel star-shaped copolymers having three different branches. *Polymer* **1992**, *33*, 2208−2213.

(2) Iatrou, H.; Hadjichristidis, N. Synthesis of a model 3-miktoarm star terpolymer. *Macromolecules* **1992**, *25*, 4649−4651.

(3) Hayashida, K.; Saito, N.; Arai, S.; Takano, A.; Tanaka, N.; Matsushita, Y. Hierarchical Morphologies Formed by ABC Star-Shaped Terpolymers. *Macromolecules* **2007**, *40*, 3695−3699.

(4) Takano, A.; Wada, S.; Sato, S.; Araki, T.; Hirahara, K.; Kazama, T.; Kawahara, S.; Isono, Y.; Ohno, A.; Tanaka, N.; Matsushita, Y. Observation of Cylinder-Based Microphase-Separated Structures from ABC Star-Shaped Terpolymers Investigated by Electron Computerized Tomography. *Macromolecules* **2004**, *37*, 9941−9946.

(5) Takano, A.; Kawashima, W.; Wada, S.; Hayashida, K.; Sato, S.; Kawahara, S.; Isono, Y.; Makihara, M.; Tanaka, N.; Kawaguchi, D.; Matsushita, Y. Composition dependence of nanophase-separated structures formed by star-shaped terpolymers of the A1.0B1.0CX type. *J. Polym. Sci., Part B: polym. Phys.* **2007**, *45*, 2277−2283.

(6) Matsushita, Y.; Hayashida, K.; Takano, A. Jewelry Box of Morphologies with Mesoscopic Length Scales − ABC Star-shaped Terpolymers. *Macromol. Rapid Commun.* **2010**, *31*, 1579−1587.
(7) Matsushita, Y.; Hayashida, K.; Dotera, T.; Takano, A. Kaleidoscopic morphologies from ABC star-shaped terpolymers. *J. Phys.: condens. Matter* **2011**, *23*, 284111.
(8) Chang, A. B.; Bates, F. S. The ABCs of Block Polymers. *Macromolecules* **2020**, *53*, 2765−2768.
(9) Hadjichristidis, N.; Iatrou, H.; Behal, S. K.; Chludzinski, J. J.; Disko, M. M.; Garner, R. T.; Liang, K. S.; Lohse, D. J.; Milner, S. T. Morphology and miscibility of miktoarm styrene-diene copolymers and terpolymers. *Macromolecules* **1993**, *26*, 5812−5815.
(10) Hückstädt, H.; Goldacker, T.; Göpfert, A.; Abetz, V. Core-Shell Double Gyroid Morphologies in ABC Triblock Copolymers with Different Chain Topologies. *Macromolecules* **2000**, *33*, 3757−3761.
(11) Moschovas, D.; Manesi, G.-M.; Karydis-Messinis, A.; Zapsas, G.; Ntetsikas, K.; Zafeiropoulos, N. E.; Piryazev, A. A.; Thomas, E. L.; Hadjichristidis, N.; Ivanov, D. A.; Avgeropoulos, A. Alternating Gyroid Network Structure in an ABC Miktoarm Terpolymer Comprised of Polystyrene and Two Polydienes. *Nanomaterials* **2020**, *10*, 1497.
(12) Hadjichristidis, N.; Iatrou, H.; Pispas, S.; Pitsikalis, M. Anionic polymerization: High vacuum techniques. *J. Polym. Sci., Part A: polym. Chem.* **2000**, *38*, 3211−3234.
(13) Uhrig, D.; Mays, J. W. Experimental techniques in high-vacuum anionic polymerization. *J. Polym. Sci., Part A: polym. Chem.* **2005**, *43*, 6179−6222.
(14) Morton, M.; Fetters, L. J. Anionic Polymerization of Vinyl Monomers. *Rubber Chem. Technol.* **1975**, *48*, 359−409.
(15) Baskaran, D.; Müller, A. H. E. Anionic vinyl polymerization—50 years after Michael Szwarc. *Prog. Polym. Sci.* **2007**, *32*, 173−219.
(16) Fontanille, M.; Gnanou, Y. *Macromolecular Engineering*; Wiley-VCH GmbH: Weinheim, Germany, 2022; pp. 1−51.
(17) Glusker, D. L.; Lysloff, I.; Stiles, E. The mechanism of the anionic polymerization of methyl methacrylate. II. The use of molecular weight distributions to establish a mechanism. *J. Polym. Sci.* **1961**, *49*, 315−334.
(18) Allen, R. D.; Long, T. E.; McGrath, J. E. Preparation of high purity, anionic polymerization grade alkyl methacrylate monomers. *Polym. Bull.* **1986**, *15*, 127−134.
(19) Wiles, D. M.; Bywater, S. Polymerization of methyl methacrylate initiated by 1,1-diphenylhexyl lithium. *Trans. Faraday Soc.* **1965**, *61*, 150−158.
(20) Mita, I.; Watabe, Y.; Akatsu, T.; Kambe, H. Anionic Polymerization of Methyl Methacrylate in Tetrahydrofuran. *Polym. J.* **1973**, *4*, 271−278.
(21) Van Beylen, M.; Bywater, S.; Smets, G.; Szwarc, M.; Worsfold, D. J. *Polysiloxane Copolymers/ Anionic Polymerization*; Springer: Berlin, Germany, 1986; pp. 87−143.
(22) Long, T. E.; Allen, R. D.; McGrath, J. E. *Recent Advances in Mechanistic and Synthetic Aspects of Polymerization*; Springer: Dordrecht, The Netherlands, 1987; pp. 79−100.
(23) Zhang, H.; Ishikawa, H.; Ohata, M.; Kazama, T.; Isono, Y.; Fujimoto, T. Anionic polymerization of alkyl methacrylates and molecular weight distributions of the resulting polymers. *Polymer* **1992**, *33*, 828−833.
(24) Sioula, S.; Tselikas, Y.; Hadjichristidis, N. Synthesis of Model 3-Miktoarm Star Terpolymers of Styrene, Isoprene, and Methyl Methacrylate. *Macromolecules* **1997**, *30*, 1518−1520.
(25) Sioula, S.; Hadjichristidis, N.; Thomas, E. L. Novel 2-Dimensionally Periodic Non-Constant Mean Curvature Morphologies of 3-Miktoarm Star Terpolymers of Styrene, Isoprene, and Methyl Methacrylate. *Macromolecules* **1998**, *31*, 5272−5277.
(26) Sioula, S.; Hadjichristidis, N.; Thomas, E. L. Direct Evidence for Confinement of Junctions to Lines in an 3 Miktoarm Star Terpolymer Microdomain Structure. *Macromolecules* **1998**, *31*, 8429−8432.
(27) Ariaee, S.; Jakobsen, B.; Norby, P.; Smilgies, D.-M.; Almdal, K.; Posselt, D. Thin film and bulk morphology of PI-PS-PMMA miktoarm star terpolymers with both weakly and strongly segregated arm pairs. *Polymer* **2023**, *283*, 126202.
(28) Kim, J.; Kim, B.; Jung, B.; Kang, Y. S.; Ha, H. Y.; Oh, I.-H.; Ihn, K. J. Effect of Casting Solvent on Morphology and Physical Properties of Partially Sulfonated Polystyrene-block-poly(ethylene-ran-butylene)-block-polystyrene Copolymers. *Macromol. Rapid Commun.* **2002**, *23*, 753−756.
(29) O'Driscoll, S.; Demirel, G.; Farrell, R. A.; Fitzgerald, T. G.; O'Mahony, C.; Holmes, J. D.; Morris, M. A. The morphology and structure of PS-b-P4VP block copolymer films by solvent annealing: effect of the solvent parameter. *Polym. Adv. Technol.* **2011**, *22*, 915−923.
(30) Huang, W.-H.; Chen, P.-Y.; Tung, S.-H. Effects of Annealing Solvents on the Morphology of Block Copolymer-Based Supramolecular Thin Films. *Macromolecules* **2012**, *45*, 1562−1569.
(31) Koide, Y.; Ikake, H.; Muroga, Y.; Shimizu, S. Effect of the cast-solvent on the morphology of cast films formed with a mixture of stereoisomeric poly(lactic acids). *Polym. J.* **2013**, *45*, 645−650.
(32) Chang, C.-Y.; Manesi, G.-M.; Yang, C.-Y.; Hung, Y.-C.; Yang, K.-C.; Chiu, P.-T.; Avgeropoulos, A.; Ho, R.-M. Mesoscale networks and corresponding transitions from self-assembly of block copolymers. *Proc. Natl. Acad. Sci. U. S. A.* **2021**, *118*, No. e2022275118.
(33) Chang, C.-Y.; Manesi, G.-M.; Wang, W.-E.; Hung, Y.-C.; Avgeropoulos, A.; Ho, R.-M. Frank-Kasper−like network phase from self-assembly of high-χ star-block copolymers. *Sci. Adv.* **2024**, *10*, No. eado4786.
(34) Gilman, H.; Cartledge, F. K. The analysis of organolithium compounds. *J. Organomet. Chem.* **1964**, *2*, 447−454.
(35) Ndoni, S.; Papadakis, C. M.; Bates, F. S.; Almdal, K. Laboratory-scale setup for anionic polymerization under inert atmosphere. *Rev. Sci. Instrum.* **1995**, *66*, 1090−1095.
(36) Höcker, H.; Lattermann, G. p-Di-(1-phenylvinyl)-Benzol und seine reaktion mit elektronenüberträgern. *Makromol. Chem.* **1972**, *158*, 191−203.
(37) Quirk, R. P.; Yoo, T. Anionic synthesis of ω-1,1-diphenylethylene-terminated polystyrene macromonomers. Rational synthesis of ABC hetero three-armed-star-branched polymers. *Polym. Bull.* **1993**, *31*, 29−36.
(38) Chernyy, S.; Mahalik, J. P.; Kumar, R.; Kirkensgaard, J. J. K.; Arras, M. M. L.; Kim, H.; Schulte, L.; Ndoni, S.; Smith, G. S.; Mortensen, K.; Sumpter, B. G.; Russell, T. P.; Almdal, K. On the morphological behavior of ABC miktoarm stars containing poly(cis 1,4-isoprene), poly(styrene), and poly(2-vinylpyridine). *J. Polym. Sci., Part B: polym. Phys.* **2018**, *56*, 1491−1504.
(39) Haas, S.; Sun, X.; Conceição, A. L. C.; Horbach, J.; Pfeffer, S. The new small-angle X-ray scattering beamline for materials research at PETRA III: SAXSMAT beamline P62. *J. Synchrotron Radiat.* **2023**, *30*, 1156−1167.
(40) Schneider, C. A.; Rasband, W. S.; Eliceiri, K. W. NIH Image to ImageJ: 25 years of image analysis. *Nat. Methods* **2012**, *9*, 671−675.
(41) Kirkensgaard, J. J. K. Kaleidoscopic tilings, networks and hierarchical structures in blends of 3-miktoarm star terpolymers. *Interface Focus* **2012**, *2*, 602−607.
(42) Kirkensgaard, J. J. K. Striped networks and other hierarchical structures in $A_mB_mC_n$ $(2m + n)$-miktoarm star terpolymer melts. *Phys. Rev. E* **2012**, *85*, 031802.
(43) Groot, R. D.; Warren, P. B. Dissipative particle dynamics: Bridging the gap between atomistic and mesoscopic simulation. *J. Chem. Phys.* **1997**, *107*, 4423−4435.
(44) Anderson, J. A.; Glaser, J.; Glotzer, S. C. HOOMD-blue: A Python package for high-performance molecular dynamics and hard particle Monte Carlo simulations. *Comput. Mater. Sci.* **2020**, *173*, 109363.
(45) Humphrey, W.; Dalke, A.; Schulten, K. VMD: Visual molecular dynamics. *J. Mol. Graphics* **1996**, *14*, 33−38.
(46) Fetters, L. J. Determination of the Intermolecular Entanglement Coupling Spacings in Polyisoprene by Viscosity Measurements. *J. Res. Natl. Bur Of Stand., Sect. A, Phys. Chem.* **1965**, *69A*, 33.

https://doi.org/10.1021/acs.macromol.6c00562
Macromolecules 2026, 59, 8285−8294

(47) Giermanska, J.; Ben Jabrallah, S.; Delorme, N.; Vignaud, G.; Chapel, J.-P. Direct experimental evidences of the density variation of ultrathin polymer films with thickness. *Polymer* **2021**, *228*, 123934.
(48) Hanley, K. J.; Lodge, T. P.; Huang, C.-I. Phase Behavior of a Block Copolymer in Solvents of Varying Selectivity. *Macromolecules* **2000**, *33*, 5918−5931.
(49) Lodge, T. P.; Pudil, B.; Hanley, K. J. The Full Phase Behavior for Block Copolymers in Solvents of Varying Selectivity. *Macromolecules* **2002**, *35*, 4707−4717.
(50) Huang, C.-I.; Hsueh, H.-Y. Phase behavior and microstructural length scales of a diblock copolymer in the presence of a selective solvent. *Polymer* **2006**, *47*, 6843−6856.
(51) Suo, T.; Yan, D.; Yang, S.; Shi, A.-C. A Theoretical Study of Phase Behaviors for Diblock Copolymers in Selective Solvents. *Macromolecules* **2009**, *42*, 6791−6798.
(52) Brandrup, J.; Immergut, E. H.; Grulke, E. A. *Polymer Handbook*; 4th ed.; Wiley: Hoboken, NJ, 1998; pp. 689−694.
(53) Xu, L.; Selin, V.; Zhuk, A.; Ankner, J. F.; Sukhishvili, S. A. Molecular Weight Dependence of Polymer Chain Mobility within Multilayer Films. *ACS Macro Lett.* **2013**, *2*, 865−868.
(54) Tcherkasskaya, O.; Ni, S.; Winnik, M. A. Direct Energy Transfer Studies of the Domain-Boundary Interface in Polyisoprene-Poly(methyl methacrylate) Block Copolymer Films. *Macromolecules* **1996**, *29*, 610−616.
(55) Eitouni, H. B.; Balsara, N. P. *Physical Properties of Polymers Handbook*; Springer: New York, USA, 2007; p 349.
(56) Khandpur, A. K.; Foerster, S.; Bates, F. S.; Hamley, I. W.; Ryan, A. J.; Bras, W.; Almdal, K.; Mortensen, K. Polyisoprene-Polystyrene Diblock Copolymer Phase Diagram near the Order-Disorder Transition. *Macromolecules* **1995**, *28*, 8796−8806.
(57) Hajduk, D. A.; Takenouchi, H.; Hillmyer, M. A.; Bates, F. S.; Vigild, M. E.; Almdal, K. Stability of the Perforated Layer (PL) Phase in Diblock Copolymer Melts. *Macromolecules* **1997**, *30*, 3788−3795.
(58) Listak, J.; Jakubowski, W.; Mueller, L.; Plichta, A.; Matyjaszewski, K.; Bockstaller, M. R. Effect of Symmetry of Molecular Weight Distribution in Block Copolymers on Formation of "Metastable" Morphologies. *Macromolecules* **2008**, *41*, 5919−5927.
(59) Groot, R. D.; Madden, T. J. Dynamic simulation of diblock copolymer microphase separation. *J. Chem. Phys.* **1998**, *108*, 8713−8724.

https://doi.org/10.1021/acs.macromol.6c00562
Macromolecules 2026, 59, 8285−8294